Impact of Nitrogen Concentration and Post-Deposition Annealing on Electrical Properties of AlON/Etched N-GaN MOS Capacitors

Pedro Fernandes Paes Pinto Rocha, Mohammed Zeghouane, Sarah Boubenia, Franck Bassani, Laura Vauche, Eugénie Martinez, William Vandendaele, Marc Veillerot, Bassem Salem

▶ **To cite this version:**

Pedro Fernandes Paes Pinto Rocha, Mohammed Zeghouane, Sarah Boubenia, Franck Bassani, Laura Vauche, et al.. Impact of Nitrogen Concentration and Post-Deposition Annealing on Electrical Properties of AlON/Etched N-GaN MOS Capacitors. Advanced Electronic Materials, 2023, 10 (3), ⟨10.1002/aelm.202300528⟩. ⟨hal-04509895⟩

HAL Id: hal-04509895
https://hal.univ-grenoble-alpes.fr/hal-04509895v1

Submitted on 20 Sep 2024

HAL is a multi-disciplinary open access archive for the deposit and dissemination of scientific research documents, whether they are published or not. The documents may come from teaching and research institutions in France or abroad, or from public or private research centers.

L'archive ouverte pluridisciplinaire **HAL**, est destinée au dépôt et à la diffusion de documents scientifiques de niveau recherche, publiés ou non, émanant des établissements d'enseignement et de recherche français ou étrangers, des laboratoires publics ou privés.

Distributed under a Creative Commons CC BY 4.0 - Attribution - International License

ADVANCED ELECTRONIC MATERIALS Open Access
www.advelectronicmat.de

Check for updates

Impact of Nitrogen Concentration and Post-Deposition Annealing on Electrical Properties of AlON/Etched N-GaN MOS Capacitors

Pedro Fernandes Paes Pinto Rocha, Mohammed Zeghouane, Sarah Boubenia, Franck Bassani, Laura Vauche, Eugénie Martinez, William Vandendaele, Marc Veillerot, and Bassem Salem**

Electrical and material properties of plasma-enhanced atomic layer deposited (PE-ALD) AlON on dry-etched *n*-type GaN substrates are investigated for nitrogen concentration ranging from 1.5% to 7.1%. Firstly, an increase in flat-band voltage (V_{FB}) and its hysteresis with increasing nitrogen concentration is reported. The increase in V_{FB} is associated with the nitrogen content whereas the increase in hysteresis to the presence of impurities (hydroxyl groups and carbon-related impurities). Alongside the nitrogen concentration, the impact of different post-deposition annealing (PDA) temperatures is studied (400–800 °C). Stable AlON layers and interfaces with etched GaN substrates are reported with slight gallium oxide growth or gallium diffusion towards the dielectric layer. Finally, with increasing PDA temperature, an increase in V_{FB} and a significant reduction of both V_{FB} hysteresis and interface state density (D_{it}) are observed, notably at the measuring temperature of 150 °C. These results present a promising pathway toward more reliable and stable normally-OFF GaN-based MOS-channel high electron mobility transistors (MOSc-HEMTs).

1. Introduction

Lateral GaN-based power devices have gained interest thanks to GaN's physical properties (wide bandgap, high breakdown voltage, high electron saturation velocity). Moreover, with the AlGaN/GaN heterojunction, high electron mobility transistors (HEMTs) can be fabricated due to a 2D electron gas (2DEG) with high mobility forming at the heterojunction. HEMTs allow high switching frequencies and low ON resistance (R_{ON}) but have a negative threshold voltage (V_{TH}).[1] The latter introduces safety issues and complicates the driver system design. HEMTs with positive V_{TH}, called normally-OFF, are hence highly desirable.

Different solutions to obtain a normally-OFF behavior exist such as the p-GaN gate,[2] the fluorinated gate,[3] and recently the double quantum well (DQW) gate structure.[4] Fully recessed Metal-Insulator-Semiconductor (MIS) gate GaN HEMTs, also called Metal-Oxide-Semiconductor-channel-HEMTs (MOSc-HEMTs), are also a promising solution to achieve normal OFF behavior. Compared to the *p*-GaN gate topology, this approach benefits from a reduced leakage current and a higher voltage swing.[5] Moreover, contrary to the partially recessed Metal-Oxide-Semiconductor (MOS) gate, the full recess of the AlGaN barrier reduces V_{TH} variation.[6]

Dielectric deposition on GaN is mandatory to fabricate the MOS gate since growing thermal Ga_2O_3 is difficult.[7] The commonly studied dielectrics are SiO_2,[8] SiN_x,[9–11] and Al_2O_3,[9,12,13] but the latter stands out thanks to its high permittivity (≈8 to 10) and high band gap (≈7 eV). However, the Al_2O_3/etched GaN gate stack suffers from V_{TH} instability due to Al_2O_3 native defects[14,15] and deteriorated interface from the necessary AlGaN barrier etching, consequently jeopardizing the implementation of MOSc-HEMTs. In order to optimize the dielectric/etched GaN gate stack, different solutions before the dielectric deposition can be implemented, ranging from surface preparation to interfacial layers.[14,16–19] After dielectric deposition, post-deposition anneal (PDA) improves the dielectric/etched GaN gate stack with

P. F. P. P. Rocha, M. Zeghouane, S. Boubenia, F. Bassani, B. Salem
Univ. Grenoble Alpes
CNRS
CEA/LETI-Minatec
Grenoble INP
LTM
Grenoble F-38054, France
E-mail: pedro.fernandespaespintorocha@cea.fr; bassem.salem@cea.fr
P. F. P. P. Rocha, L. Vauche, E. Martinez, W. Vandendaele, M. Veillerot
Univ. Grenoble Alpes
CEA
Leti
Grenoble F-38000, France

The ORCID identification number(s) for the author(s) of this article can be found under https://doi.org/10.1002/aelm.202300528

© 2023 The Authors. Advanced Electronic Materials published by Wiley-VCH GmbH. This is an open access article under the terms of the Creative Commons Attribution License, which permits use, distribution and reproduction in any medium, provided the original work is properly cited.

DOI: 10.1002/aelm.202300528

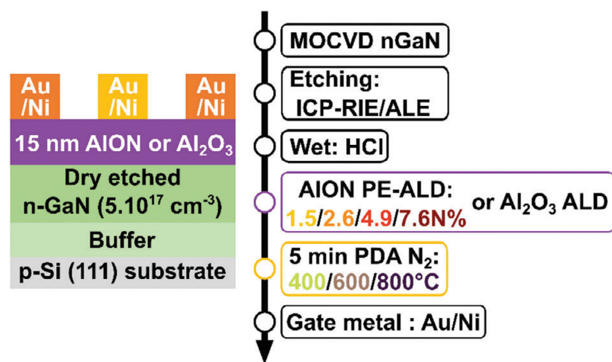

Figure 1. Cross-sectional schematic representation of the fabricated MOS capacitors with its process flow.

reduced V_{TH} hysteresis and increased V_{TH}.[12,20] Nonetheless, the low thermal stability of Al_2O_3 deposited on GaN limits the use of high-temperature PDA.[21,22]

There has been a growing interest in aluminum oxynitride (AlO_xN_y) for improved dielectric/GaN stack. The incorporation of nitrogen in Al_2O_3 was indeed reported to generate fixed negative charges allowing for an increase in the flat-band voltage (V_{FB}), reducing electron trapping into the dielectric layer, and presenting a better dielectric/GaN interface.[23–32] The thermal stability for AlON deposited on AlGaN is also reported to increase up to 800 °C.[24] Moreover, similarly to Al_2O_3, annealing was reported to increase V_{FB} and reduce its hysteresis for annealing under forming gas and O_2.[23,26] If some reports discuss the benefits of using AlON on MOSc-HEMT after a high temperature,[29,30] few studies present a systematic analysis of the electrical properties of the AlON/etched GaN stack for different nitrogen concentrations and after different PDA temperatures.

We have recently reported the indirect growth of plasma-enhanced atomic layer deposited (PE-ALD) AlON on etched GaN substrate with controlled nitrogen concentration,[33] with the O_2 plasma oxidation step expected to lower the presence of impurities.[34,35] This work reports the impact of different nitrogen concentrations and PDA temperatures for PE-ALD AlON/etched *n*-GaN gate stack through electrical measurements at 25 and 150 °C alongside physical-chemical measurements.

2. Results and Discussion

2.1. Impact of Nitrogen Concentration

AlON with different nitrogen concentrations ranging from 1.5 to 7.1 N% were studied with planar MOS capacitors (MOSCAPs) together with a reference Al_2O_3 (H_2O-based ALD) (**Figure 1**). In this section, the impact of the different nitrogen concentrations in AlON was investigated without PDA. **Figure 2** shows the *C*–*V* and $G_m/\omega - V$ characteristics measured at 25 and 150 °C for the reference Al_2O_3 and the AlON samples with different nitrogen concentrations. For AlON, *C*–*V* characteristics are shifted positively with higher nitrogen concentration as previously reported,[23,25] but the shift does not go beyond Al_2O_3 for both measuring temperatures. A double slope at AlON's *C*–*V* characteristics is also observed at 25 °C but disappears at 150 °C. This slope seems to be related to interface states since conductance peaks are observed close to the slope. By increasing the temperature, deeper interface states can respond to the *C*–*V* measurement while their emission time is reduced according to the Shockley–Read–Hall (SRH) model, thus leading to the disappearance of the slope. All studied samples present clockwise hysteresis. It increases at 150 °C compared to 25 °C due to electron trapping in the oxide and at the interface being enhanced by the elevated temperature. Among all samples, Al_2O_3 has the highest hysteresis for 150 °C.

From the *C*–*V* characteristics, the V_{FB} and ΔV_{FB} are extracted and shown in **Figure 3**. As mentioned before for AlON, the increased V_{FB} with higher nitrogen concentration is noticed for both measuring temperatures. Hysteresis seems to be slightly impacted by nitrogen content as ΔV_{FB} increases for a nitrogen concentration higher than 1.5% at both 25 and 150 °C. However, no clear trend with nitrogen concentration can be observed. Nonetheless, at both measuring temperatures, the lower hysteresis of AlON samples compared to Al_2O_3 seems to indicate that nitrogen incorporation in AlON indeed reduces electron trapping, especially for the higher measuring temperature of 150 °C. The lower electron trapping for AlON could be explained by the reduction of oxygen vacancies (V_O)[28] and/or the increase of conduction band off-set between AlON and GaN,[30] although AlON's band gap is reported to be slightly smaller than Al_2O_3.[24,27]

In terms of interface quality, the interface state density (D_{it}) at both measuring temperatures is extracted from the conductance peaks using the methodology by Vandendaele et al.[36] From Equation (1), with a frequency of 1 kHz and at both measuring temperatures of 25 and 150 °C, the extracted defect energy levels from the conduction band are around 0.49 and 0.71 eV, respectively.

$$E_C - E_T = kT.\ln\left(\frac{2\nu_t\sigma_s N_C}{2\pi f}\right) \quad (1)$$

where *k* is the Boltzmann constant, *T* the temperature, ν_t the thermal velocity, σ_s the electron capture cross-section, N_C the effective density of states in GaN's conduction band, and *f* the frequency. σ_s was assigned to 1×10^{-14} cm^{-2}, ν_t to 2.6×10^7cm.s^{-1}, and to 3.1×10^7cm.s^{-1} for 25 and 150 °C, respectively. Although the GaN surface is etched, the results summarized in **Table 1** show an overall better interface for the AlON/GaN interface, as previously observed,[29,30] specifically when nitrogen concentration is reduced, whereas the interface states density for 7.1 N% AlON is close to Al_2O_3. As such, the increase in nitrogen concentration induces a small degradation of the AlON/GaN interface.

Therefore, when compared to Al_2O_3, the insertion of nitrogen at a concentration lower than 5% seems to improve the quality of both the dielectric and the interface with reduced hysteresis and interface states. However, within the AlON samples, the increase in nitrogen concentration leads to deterioration. This is contrary to the reported literature, where an increase in nitrogen incorporation leads to lower electron trapping.[27] To further understand the impact of nitrogen on the V_{FB} hysteresis and D_{it}, ToF-SIMS analyses were carried out on the AlN reference sample, 2.6, 4.9, and 7.1 N% AlON samples. As shown in **Figure 4**, ToF-SIMS analyses reveal with higher nitrogen content an increase in hydroxyl groups and carbon impurities. The deteriorated hysteresis and D_{it} with increasing nitrogen concentration could be related to the

 © 2023 The Authors. Advanced Electronic Materials published by Wiley-VCH GmbH

2199160x, 2024, 3, Downloaded from https://onlinelibrary.wiley.com/doi/10.1002/aelm.202300528 by Cea Grenoble, Wiley Online Library on [20/09/2024]. See the Terms and Conditions (https://onlinelibrary.wiley.com/terms-and-conditions) on Wiley Online Library for rules of use; OA articles are governed by the applicable Creative Commons License

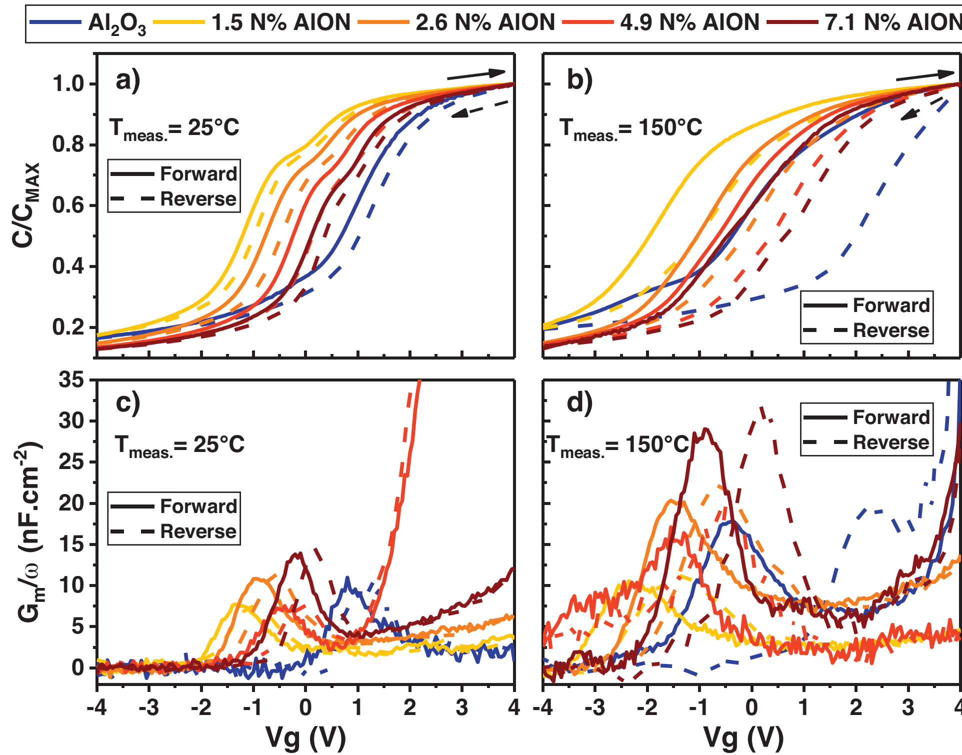

Figure 2. *C–V* characteristics for Al_2O_3 and AlON samples without annealing at the measuring temperatures of a) 25 and b) 150 °C (median of three measurements); G_m/ω characteristics at c) 25 and d) 150 °C (single measurement).

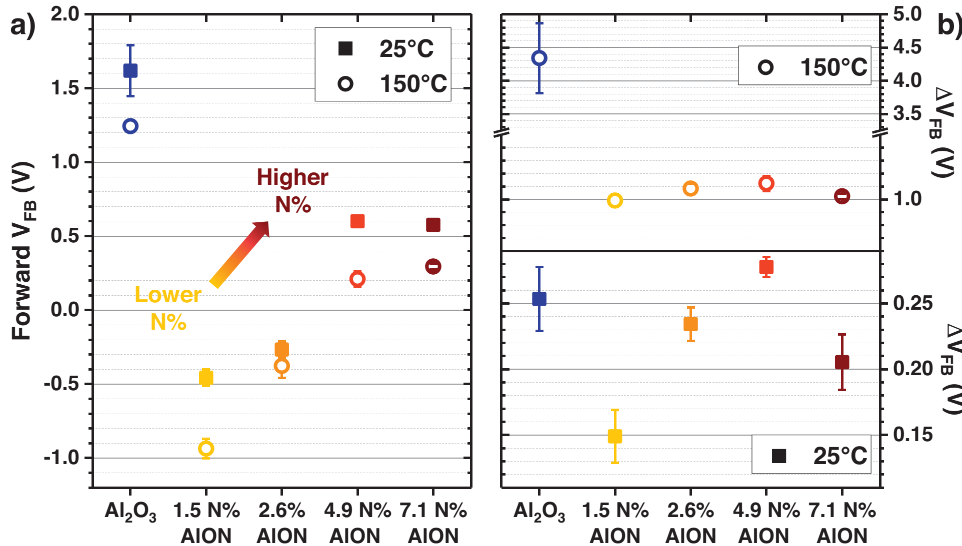

Figure 3. a) Extracted forward V_{FB} at the measuring temperatures of 25 and 150 °C; b) Extracted V_{FB} hysteresis at 25 and 150 °C.

Table 1. Interface states density extracted from G_m/ω peaks at 1 kHz for both 25 and 150 °C.

E_C-E_T [eV]	Al_2O_3	1.5 N% AlON	2.6 N% AlON	4.9 N% AlON	7.1 N% AlON [10^{11} $eV^{-1}.cm^{-2}$]
0.49 (25 °C)	2.50 ± 0.35	0.95 ± 0.08	1.82 ± 0.11	1.33 ± 0.01	2.25 ± 0.11
0.72 (150 °C)	4.98 ± 0.74	1,86 ± 0.05	2.82 ± 0.16	2.73 ± 0.07	5.72 ± 0.54

© 2023 The Authors. Advanced Electronic Materials published by Wiley-VCH GmbH

2199160x, 2024, 3, Downloaded from https://onlinelibrary.wiley.com/doi/10.1002/aelm.202300528 by Cea Grenoble, Wiley Online Library on [20/09/2024]. See the Terms and Conditions (https://onlinelibrary.wiley.com/terms-and-conditions) on Wiley Online Library for rules of use; OA articles are governed by the applicable Creative Commons License

increase of hydroxyl groups and carbon impurities, as previously reported.[22,37,38] The increase of these impurities seems not to be directly related to the nitrogen concentration but mostly to the deposition technique, especially for carbon impurities. In order to obtain lower nitrogen concentration, thinner AlN layers have to be oxidized, meaning that fewer carbon impurities from AlN deposition remain in the AlON layer. As for hydroxyl groups, no particular explanation was found for their increase with respect to the nitrogen concentration.

Thus, in comparison with Al_2O_3, the introduction of nitrogen for all concentrations is more advantageous specifically for high operating temperatures. However, within AlON samples, lower nitrogen concentrations have lower electron trapping due to the lower presence of impurities.

2.2. Impact of PDA

After post-deposition annealing, **Figure 5** shows the *C–V* and G_m/ω characteristics for different nitrogen content in AlON after a PDA at 800 °C. The Al_2O_3 characteristics were not measured due to the large leakage current from crystallization after an 800 °C PDA. The presence of *C–V* characteristics for AlON confirms the higher thermal stability of AlON over Al_2O_3 thanks to the introduction of nitrogen in aluminum oxide. Moreover, the positive shift of *C–V* curves with higher nitrogen concentration is also noticed after PDA, and at both measuring temperatures. Hysteresis reduces with the PDA temperature, as previously reported for a PDA under forming gas or O_2.[23,26] Concerning the interface, conductance peaks are reduced for the different nitrogen concentrations and at both measuring temperatures, leading to the disappearance of the slope observed for the AlON samples without PDA. The oxide capacitance and permittivity at 800 °C are represented in **Table 2**. The permittivity is between 8.7 to 10.5, in the range of reported permittivity for Al_2O_3.[39,40]

The extracted V_{FB} and hysteresis at both measuring temperatures and for different PDA temperatures are shown in **Figure 6**. While nitrogen incorporation increases the V_{FB}, PDA also increases V_{FB} as previously reported for PDA under O_2 on

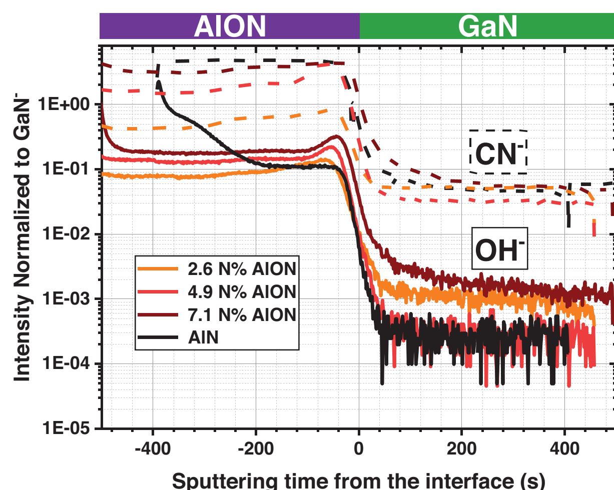

Figure 4. Normalized ToF-SIMS analyses of CN^- and OH^- depth profiles for a reference AlN sample, 2.6 N%, 4.9 N%, and 7.1 N% AlON samples.

Table 2. Oxide capacitance and permittivity for samples annealed at 800 °C (median of three measurements).

	1.5 N% AlON	2.6 N% AlON	4.9 N% AlON	7.1 N% AlON
C_{OX} [nF.cm^{-2}]	513.3	542.8	619.5	548.7
ϵ_{OX}	8.7	9.2	10.5	9.3

AlON.[26] In our case, PDA increases and stabilizes V_{FB} throughout the different annealing temperatures, especially for nitrogen concentrations under 4.9%. On the other side, V_{FB} for Al_2O_3 is strongly reduced with increasing PDA temperature, with a V_{FB} being lower than AlON for a 600 °C PDA. As mentioned, hysteresis for all samples reduces for both measuring temperatures. At 25 °C, ΔV_{FB} reduction for Al_2O_3, 1.5 N%, and 2.6 N% AlON follows a similar trend and stays below 4.9 and 7.1 N% AlON samples. However, at 150 °C, a more pronounced hysteresis is observed for Al_2O_3, while AlON samples have a lower hysteresis. This observation further confirms the reduction of electron trapping by nitrogen incorporation. Interestingly, hysteresis for 1.5 and 2.6 N% are strongly reduced even at 150 °C, with a low hysteresis for both measuring temperatures.

Concerning the AlON/GaN interface electrical properties, a reduction of D_{it} with PDA temperature is observed for AlON samples. D_{it} is only reduced for Al_2O_3 after a 400 °C PDA (**Figure 7**). At the defect energy level of 0.49 eV, little difference is noticed between the AlON samples. But for an 800 °C PDA, a lower interface state density is found for 1.5 N% AlON. The same observation is made at 0.72 eV where D_{it} is lower for 1.5 and 2.6 N% AlON. Hence, with a lower nitrogen concentration and a PDA temperature higher than 600 °C, a better interface is obtained for the AlON/etched GaN stack.

In order to verify the nitrogen content and distribution in the AlON after PDA, HAXPES, and ToF-SIMS were performed using the 4.9 N% AlON sample for its intermediary nitrogen content. As shown in **Table 3**, a stable nitrogen concentration is found for the different PDA temperatures, highlighting stable nitrogen incorporation within AlON even after 800 °C PDA, similar to AlON deposited by Nozaki et al. After 800 °C.[27] The difference in nitrogen content from the expected value of 4.9N% can be associated with the uncertainty of the fitting process used to take away the N-Ga contribution from the GaN substrate.

GIXRD analyses of annealed AlON samples at 900 °C (see Figure S4, Supporting Information) also confirm the stability of the dielectric layer with no sign of crystallization for a PDA at 900 °C.

Regarding the interfacial gallium oxide, AR-HAXPES for 1.5N% AlON samples shown in **Figure 8** reveals a slight increase

Table 3. The atomic percentage for N, Al, and O in 4.9 N% AlON by using quantification with HAXPES.

PDA temperature [°C]	N	Al	O [at %]
w/o PDA	4.1	33.7	62.2
400	4.8	32.8	62.4
600	4.4	33.5	62.2
800	4.2	33.3	62.5

© 2023 The Authors. Advanced Electronic Materials published by Wiley-VCH GmbH

2199160x, 2024, 3, Downloaded from https://onlinelibrary.wiley.com/doi/10.1002/aelm.202300528 by Cea Grenoble, Wiley Online Library on [20/09/2024]. See the Terms and Conditions (https://onlinelibrary.wiley.com/terms-and-conditions) on Wiley Online Library for rules of use; OA articles are governed by the applicable Creative Commons License

2199160x, 2024, 3, Downloaded from https://onlinelibrary.wiley.com/doi/10.1002/aelm.202300528 by Cea Grenoble, Wiley Online Library on [20/09/2024]. See the Terms and Conditions (https://onlinelibrary.wiley.com/terms-and-conditions) on Wiley Online Library for rules of use; OA articles are governed by the applicable Creative Commons License

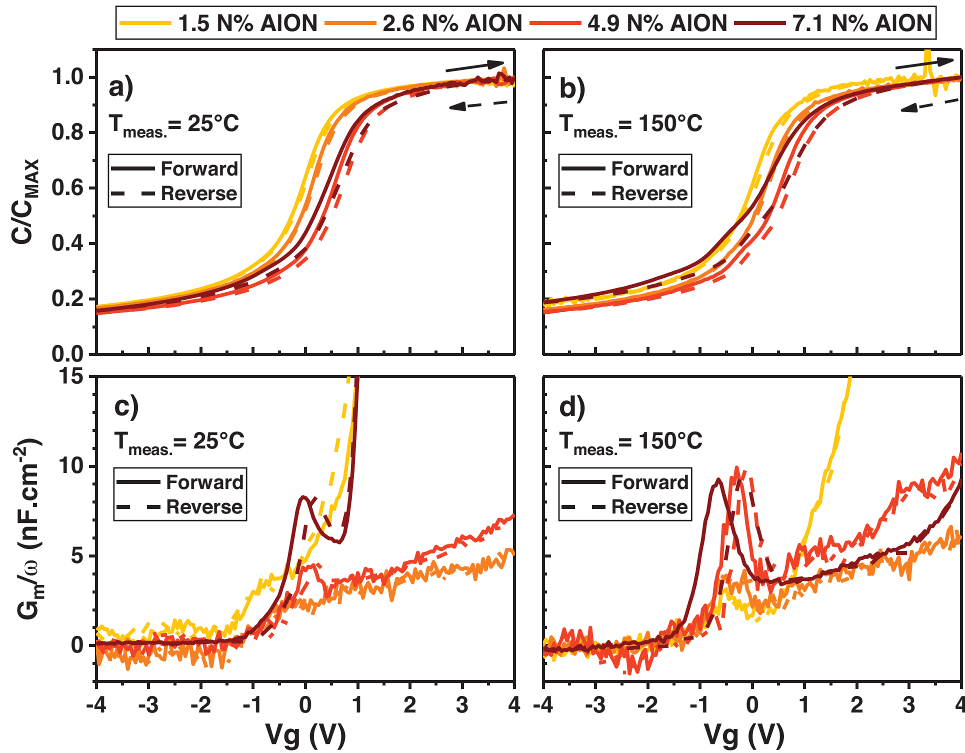

Figure 5. *C–V* characteristics for AlON samples with 800 °C PDA at the measuring temperatures of a) 25 and b) 150 °C (median of three measurements); G_m/ω characteristics at c) 25 and d) 150 °C (single measurement).

in oxidation at the AlON/GaN interface with increasing PDA temperature. However, the thickness remains under 1 nm. The observed overall stability of AlON with high-temperature annealing is consistent with a previous report of AlON on AlGaN,[24] in our case both the AlON layer and the interface proven to be stable for high-temperature PDA above 600 °C on etched GaN surface. This absence of significant growth of interfacial gallium oxide correlates to the stable and improved interface discussed previously.

Finally, in **Figure 9**, the ToF-SIMS analyses of the AlON/etched GaN stack are represented. The AlN^- profiles confirm the absence of a degraded layer or inhomogeneous nitrogen distribution with increasing PDA temperatures. Concerning the interface stability, ToF-SIMS analyses of GaO^- profiles also confirm minor growth of GaO_x or gallium diffusion with increasing PDA temperature. The observed reduction of hydroxyl groups with increasing PDA temperature could partially explain the reduction

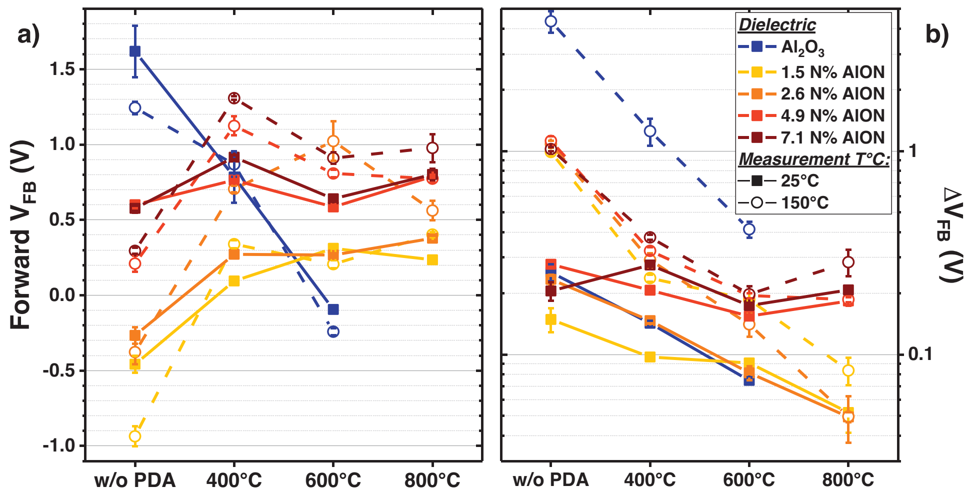

Figure 6. For the different PDA temperatures: a) Extracted forward V_{FB} at the measuring temperatures of 25 and 150 °C; b) Extracted V_{FB} hysteresis at 25 and 150 °C.

© 2023 The Authors. Advanced Electronic Materials published by Wiley-VCH GmbH

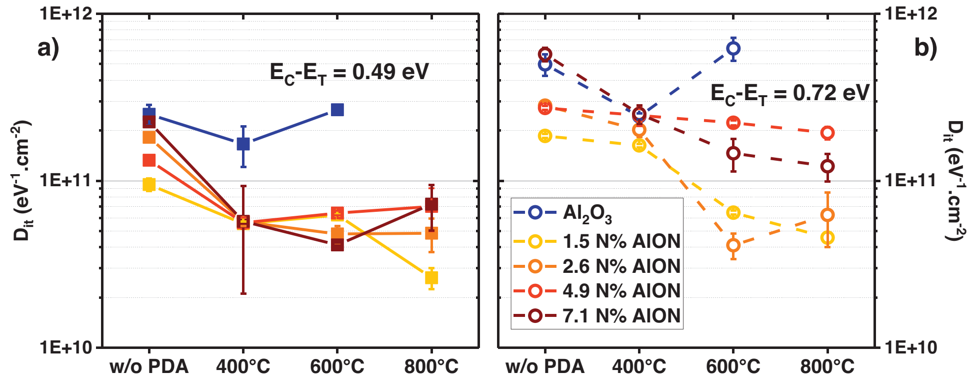

Figure 7. Interface states density extracted from G_m/ω peaks at 1 kHz at both measuring temperatures of a) 25 and b) 150 °C for Al_2O_3 and AlON samples with different PDA temperatures.

of hysteresis with PDA temperature.[37,22] Possible other defects such as border traps in the dielectric layer[20,41] could also be reduced by the PDA process. However, the carbon impurities do not reduce with PDA. This means that they are well incorporated within the AlON layer and cannot explain the ΔV_{FB} reduction with the PDA temperature. Assuming that the carbon content for the other nitrogen concentration has the same behavior, this assumption could explain the difference observed between the different AlON samples even after PDA.

3. Conclusion

In this work, the impacts of different nitrogen concentrations in AlON and post-deposition annealing were investigated and compared to Al_2O_3 using electrical and physical-chemical characterizations.

Without annealing, an increase of V_{FB} with nitrogen content was observed, consistent with the literature. Hysteresis is well improved by the presence of nitrogen when compared to Al_2O_3, especially for a measuring temperature of 150 °C. The increase of electron trapping with nitrogen seems to originate from the presence of impurities related to the deposition technique.

With annealing, stable AlON layers and interfaces with etched GaN were observed for PDA temperatures up to 800 °C. When combined with low nitrogen content, V_{FB} was increased and stabilized. The V_{FB} hysteresis was strongly reduced by PDA for AlON and Al_2O_3 samples thanks partly to the hydroxyl groups' reduction. In addition, AlON exhibited a lower hysteresis than Al_2O_3 at 150 °C while having a lower D_{it}, highlighting the superior electrical properties of AlON and its interface with etched GaN. Considering hysteresis and interface quality at both measuring temperatures, the more suitable nitrogen concentrations are around 1.5 and 2.6% with an annealing between 600 and 800 °C.

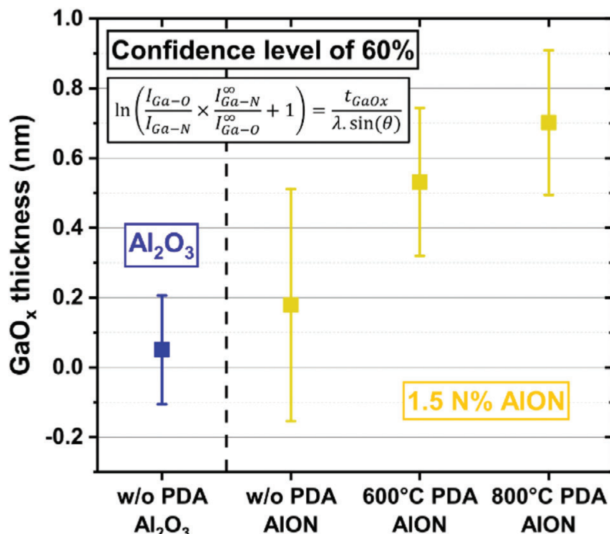

Figure 8. Interfacial GaO_X thickness obtained by AR-HAXPES using three take-off angles (42/50/65°) for Al_2O_3 and with 1.5 N% AlON without PDA, with 600 and 800 °C PDA.

4. Experimental Section

Device Fabrication: 200 mm *n*-GaN buffer layers with (0001) orientation were grown on *p*-Si (111) substrates by metal-organic chemical vapor deposition (MOCVD). The *n*-type doping concentration was about 5 × 10^{17} cm^{-3}. To simulate the fully recessed GaN HEMT's gate bottom, the substrate underwent dry-etching by inductively coupled plasma reactive ion etching (ICP-RIE) and atomic layer etching (ALE). Samples of 1.5 × 1.5 cm^2 were cleaved and cleaned with HCl for 3 min, rinsed with deionized water, and then dried with N_2. 15 nm of AlON with different nitrogen concentrations were deposited by PE-ALD in a supercycle approach, with the precursors for Al, N, and O being trimethylaluminium (TMA), N_2 plasma, and O_2 plasma, respectively. In this approach, for one AlON cycle, thin PE-ALD AlN layers were oxidized by an O_2 plasma for 15 s. The AlN deposition cycle consists of TMA injection for 0.05 s, Ar purge for 3 s, N_2 plasma for 15 s, and again Ar purge for 3 s. In order to control the nitrogen concentration, different AlN thicknesses were oxidized. The concentrations were fixed at 1.5%, 2.6%, 4.9%, and 7.1% in atomic concentration. 15 nm of Al_2O_3 was deposited by ALD for the reference sample, with TMA and H_2O as precursors. The deposition temperature was 300 °C for both dielectrics. After deposition, PDA was performed under N_2 for 5 min at 400, 600, and 800 °C for both AlON and Al_2O_3 samples. Circular MOSCAP structures were fabricated for electrical measurements with Ni/Au deposited by e-beam evaporation as in our previous work.[42] The diameter of the circular gate contact was 100 or 200 µm.

Electrical and Physical-Chemical Characterizations: Back-to-back *C–V* measurements were carried out at 1 kHz with a forward voltage sweep

 © 2023 The Authors. Advanced Electronic Materials published by Wiley-VCH GmbH

2199160x, 2024, 3, Downloaded from https://onlinelibrary.wiley.com/doi/10.1002/aelm.202300528 by Cea Grenoble, Wiley Online Library on [20/09/2024]. See the Terms and Conditions (https://onlinelibrary.wiley.com/terms-and-conditions) on Wiley Online Library for rules of use; OA articles are governed by the applicable Creative Commons License

2199160x, 2024, 3, Downloaded from https://onlinelibrary.wiley.com/doi/10.1002/aelm.202300528 by Cea Grenoble, Wiley Online Library on [20/09/2024]. See the Terms and Conditions (https://onlinelibrary.wiley.com/terms-and-conditions) on Wiley Online Library for rules of use; OA articles are governed by the applicable Creative Commons License

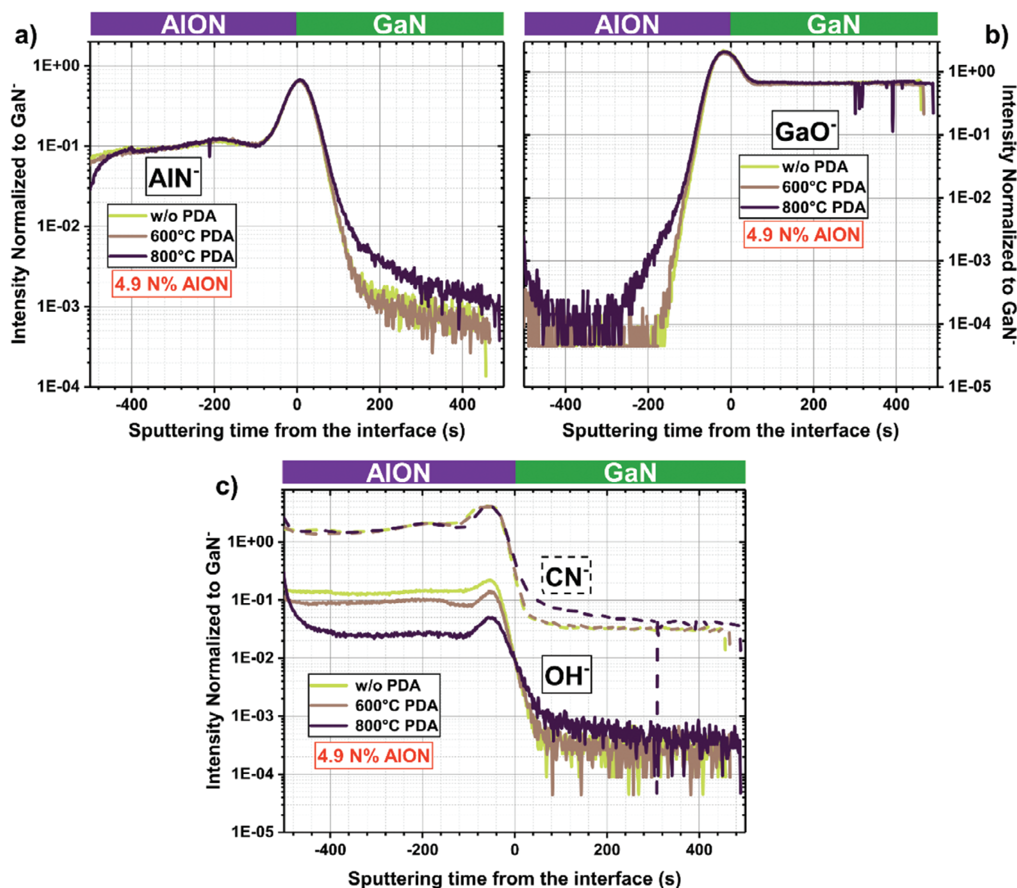

Figure 9. Normalized ToF-SIMS analyses of a) AlN^-, b) GaO^-, and c) both CN^- and OH^- depth profiles for 4.9 N% AlON samples without PDA and with respectively 600 and 800 °C PDA.

between -4 V and 4 V, and a backward voltage sweep between 4 and −4 V. The V_{FB} was extracted by calculating the flat-band capacitance (C_{FB}) as in Equation (2).

$$C_{FB} = C_{OX}C_D/(C_{OX}+C_D) \text{with } C_D=\sqrt{kT\epsilon_{GaN}\epsilon_0/(q^2N_D)} \quad (2)$$

where C_{ox}, k, T, ϵ_{GaN}, ϵ_0, and q are respectively the oxide capacitance, the Boltzmann constant, the temperature in Kelvin, the relative GaN permittivity, the vacuum permittivity, and the electron elementary charge. The nitrogen atomic concentration and the interfacial gallium oxide thickness were analyzed by hard X-ray photoelectron spectroscopy (HAXPES) and angle-resolved HAXPES (AR-HAXPES) respectively. Both HAXPES and AR-HAXPES analyses were performed using PHI Quantes equipped with a monochromatic Cr $K\alpha$ ($h\nu$ = 5414.7 eV) X-ray source which allowed the analysis of buried interfaces. The photoelectron take-off angle for HAXPES analyses was 45°. Since the C1s spectrum intensity was strongly reduced with the Cr $K\alpha$ source, the binding energy was calibrated with Al1s binding energy at 1562 eV.[43] Three contributions for the N1s spectrum were used: N-Ga at around 398 eV, O-N-Al at 399.7 eV,[23,30,44,45] and N–O at 403 eV.[23,27,30,45] For AR-HAXPES, the different analyzed angles were 42°, 50°, and 65°. The binding energy calibration for AR-HAXPES was performed using $Ga2p_{3/2'}$s binding energy at 65°, which corresponded to the angle having the most signal from GaN's bulk (information depth of ≈5 nm for 65° against ≈0.38 nm for 42° in the GaN substrate). Three contributions were used: Ga-N at around ≈1117 to 1118 eV, Ga-O at ≈1117.7 to 1118.7 eV, and Ga-Ga at ≈1115.7 to 1116.3 eV. The energy shift between Ga-N and Ga-O was fixed at 0.7 eV[46] while the shift between Ga-N and Ga-Ga was fixed at −1.3 eV.[47] With AR-HAXPES, the interfacial GaO_x thickness was calculated using Equation (3).

$$\ln\left(\frac{I_{Ga-O}}{I_{Ga-N}} \times \frac{I^{\infty}_{Ga-N}}{I^{\infty}_{Ga-O}} + 1\right) = \frac{t_{GaOx}}{\lambda.\sin(\theta)} \quad (3)$$

where $I_{Ga\text{-}O}$ and $I_{Ga\text{-}N}$ are the measured Ga-O and Ga-N peaks' intensity respectively, I^{∞}_{Ga-O} and I^{∞}_{Ga-N} the Ga-O and Ga-N peaks' intensity in bulk respectively. The ratio $I^{\infty}_{Ga-N}/I^{\infty}_{Ga-O}$ was experimentally extracted as 0.873. λ was the inelastic mean free path in Ga_2O_3 assigned at 5.831 nm using the TPP-2 model[48] and θ was the photoelectron take-off angle. The estimated GaO_x thickness t_{GaOx} was obtained by linear extrapolation of Equation (3) (see Figure S3, Supporting Information). Both HAXPES and AR-HAXPES spectra are represented in the Supporting Information (see Figures S1 and S2, Supporting Information). The nitrogen distribution and impurities were analyzed by ToF-SIMS analyses using a TOF-SIMS 5 with a 500 eV Cs^+ sputter gun and by detecting negative secondary ions, obtained from a $Bi_3{}^+$ ions analytical beam, energized at 15 kV. The intensity was normalized with the bulk GaN^- signal while the sputtering time was adjusted to start at the dielectric/GaN interface of each sample where the GaN^- signal was reduced by 50% compared to the bulk signal. Specifically for ToF-SIMS, an AlN reference sample was deposited by PE-ALD using TMA and N_2 plasma.

© 2023 The Authors. Advanced Electronic Materials published by Wiley-VCH GmbH

Supporting Information

Supporting Information is available from the Wiley Online Library or from the author.

Acknowledgements

The authors are grateful to M. Charles for the epitaxy and S. Ruel for the etching. This work was partly supported by the French RENATECH network through the PTA technological platforms in Grenoble, by the "Recherches Technologiques de base" program of the French National Research Agency (ANR) regarding the HAXPES, AR-HAXPES, and ToF-SIMS analyses and has received a partial funding from IPCEI/Nano2026.

Conflict of Interest

The authors declare no conflict of interest.

Data Availability Statement

The data that support the findings of this study are available from the corresponding author upon reasonable request.

Keywords

AlON, GaN, interfaces, Metal-Oxide-Semiconductor capacitor, post-deposition anneal

Received: August 4, 2023
Revised: November 16, 2023
Published online: December 7, 2023

[1] J. He, W.-C. Cheng, Q. Wang, K. Cheng, H. Yu, Y. Chai, *Adv. Electron. Mater.* **2021**, *7*, 2001045.
[2] G. Greco, F. Iucolano, F. Roccaforte, *Mater. Sci. Semicond. Process.* **2018**, *78*, 96.
[3] S. Jia, Y. Cai, D. Wang, B. Zhang, K. M. Lau, K. J. Chen, *Phys. Status Solidi C* **2006**, *3*, 2368.
[4] D. Biswas, T. Tsuboi, T. Egawa, *Mater. Sci. Semicond. Process.* **2021**, *135*, 106109.
[5] C. L. Royer, B. Mohamad, J. Biscarrat, L. Vauche, R. Escoffier, J. Buckley, S. Bécu, R. Riat, C. Gillot, M. Charles, S. Ruel, P. Pimenta-Barros, N. Posseme, P. Besson, F. Boudaa, C. Vannuffel, W. Vandendaele, A. G. Viey, A. Krakovinsky, M.-A. Jaud, R. Modica, F. Iucolano, R. L. Tiec, S. Levi, M. Orsatelli, R. Gwoziecki, V. Sousa, in *2022 IEEE 34th Int. Symp. on Power Semiconductor Devices and ICs (ISPSD)*, IEEE, Vancouver, BC, Canada **2022**, pp. 49–52. https://doi.org/10.1109/ISPSD49238.2022.9813672
[6] H. Amano, Y. Baines, E. Beam, M. Borga, T. Bouchet, P. R. Chalker, M. Charles, K. J. Chen, N. Chowdhury, R. Chu, C. De Santi, M. M. De Souza, S. Decoutere, L. Di Cioccio, B. Eckardt, T. Egawa, P. Fay, J. J. Freedsman, L. Guido, O. Häberlen, G. Haynes, T. Heckel, D. Hemakumara, P. Houston, J. Hu, M. Hua, Q. Huang, A. Huang, S. Jiang, H. Kawai, et al., *J. Phys. D: Appl. Phys.* **2018**, *51*, 163001.
[7] T. Yamada, J. Ito, R. Asahara, K. Watanabe, M. Nozaki, S. Nakazawa, Y. Anda, M. Ishida, T. Ueda, A. Yoshigoe, T. Hosoi, T. Shimura, H. Watanabe, *J. Appl. Phys.* **2017**, *121*, 035303.
[8] P. Fiorenza, G. Greco, F. Iucolano, A. Patti, F. Roccaforte, *IEEE Trans. Electron Devices* **2017**, *64*, 2893.
[9] T.-L. Wu, D. Marcon, B. Bakeroot, B. De Jaeger, H. C. Lin, J. Franco, S. Stoffels, M. Van Hove, R. Roelofs, G. Groeseneken, S. Decoutere, *Appl. Phys. Lett.* **2015**, *107*, 093507.
[10] M. Hua, Z. Zhang, J. Wei, J. Lei, G. Tang, K. Fu, Y. Cai, B. Zhang, K. J. Chen, in *IEEE Int. Electron Devices Meeting (IEDM)*, IEEE, San Francisco, CA **2016**, pp. 10.4.1–10.4.4. https://doi.org/10.1109/IEDM.2016.7838388
[11] W. Shi, Q. Jiang, T. Luan, S. Huang, X. Wang, F. Guo, Y. Yao, K. Deng, L. Bi, J. Fan, H. Yin, K. Wei, W. Xiong, Y. Li, H. Jiang, J. Li, X. Liu, *IEEE Trans. Electron Devices* **2021**, *68*, 4274.
[12] Q. Zhou, L. Liu, A. Zhang, B. Chen, Y. Jin, Y. Shi, Z. Wang, W. Chen, B. Zhang, *IEEE Electron Device Lett.* **2016**, *37*, 165.
[13] D. Biswas, N. Torii, H. Fujita, T. Yoshida, T. Kubo, T. Egawa, *Semicond. Sci. Technol.* **2019**, *34*, 055014.
[14] Q. Wang, Y. Jiang, J. Zhang, K. Kawaharada, L. Li, D. Wang, J.-P. Ao, *Semicond. Sci. Technol.* **2015**, *30*, 065004.
[15] A. G. Viey, W. Vandendaele, M.-A. Jaud, L. Gerrer, X. Garros, J. Cluzel, S. Martin, A. Krakovinsky, J. Biscarrat, R. Gwoziecki, M. Plissonnier, F. Gaillard, R. Modica, F. Iucolano, M. Meneghini, G. Meneghesso, G. Ghibaudo, *IEEE Trans. Electron Devices* **2021**, *68*, 2017.
[16] L. Vauche, A. Chanuel, E. Martinez, M.-C. Roure, C. Le Royer, S. Bécu, R. Gwoziecki, M. Plissonnier, *ACS Appl. Electron. Mater.* **2021**, *3*, 1170.
[17] S. Benrabah, M. Legallais, P. Besson, S. Ruel, L. Vauche, B. Pelissier, C. Thieuleux, B. Salem, M. Charles, *Appl. Surf. Sci.* **2022**, *582*, 152309.
[18] S. Liu, S. Yang, Z. Tang, Q. Jiang, C. Liu, M. Wang, B. Shen, K. J. Chen, *Appl. Phys. Lett.* **2015**, *106*, 051605.
[19] M. Hua, X. Cai, S. Yang, Z. Zhang, Z. Zheng, J. Wei, N. Wang, K. J. Chen, in *IEEE Int. Electron Devices Meeting (IEDM)*, IEEE, San Francisco, CA **2018**, pp. 30.3.1–30.3.4.
[20] T. Kubo, M. Miyoshi, T. Egawa, *Semicond. Sci. Technol.* **2017**, *32*, 065012.
[21] Y. Hori, C. Mizue, T. Hashizume, *Jpn. J. Appl. Phys.* **2010**, *49*, 080201.
[22] P. Fernandes Paes Pinto Rocha, L. Vauche, B. Mohamad, W. Vandendaele, E. Martinez, M. Veillerot, T. Spelta, N. Rochat, R. Gwoziecki, B. Salem, V. Sousa, *Power Electron. Devices Compon.* **2023**, *4*, 100033.
[23] M. A. Negara, M. Kitano, R. D. Long, P. C. Mcintyre, *ACS Appl. Mater. Interfaces* **2016**, *8*, 21089.
[24] R. Asahara, M. Nozaki, T. Yamada, J. Ito, S. Nakazawa, M. Ishida, T. Ueda, A. Yoshigoe, T. Hosoi, T. Shimura, H. Watanabe, *Appl. Phys. Express* **2016**, *5*, 101002.
[25] Q. Wang, X. Cheng, L. Zheng, L. Shen, J. Li, D. Zhang, R. Qian, Y. Yu, in *2017 29th Int. Symp. on Power Semiconductor Devices and IC's (ISPSD)*, IEEE, Sapporo, Japan **2017**, pp. 215–218. https://doi.org/10.23919/ISPSD.2017.7988926
[26] S. Nakazawa, H.-A. Shih, N. Tsurumi, Y. Anda, T. Hatsuda, T. Ueda, M. Nozaki, T. Yamada, T. Hosoi, T. Shimura, H. Watanabe, T. Hashizume, in *2017 IEEE Int. Electron Devices Meeting (IEDM)*, IEEE, San Francisco, CA **2017**, pp. 25.1.1–25.1.4. https://doi.org/10.1109/IEDM.2017.8268455
[27] M. Nozaki, K. Watanabe, T. Yamada, H.-A. Shih, S. Nakazawa, Y. Anda, T. Ueda, A. Yoshigoe, T. Hosoi, T. Shimura, H. Watanabe, *Jpn. J. Appl. Phys.* **2018**, *57*, 06KA02.
[28] E. Kojima, K. Chokawa, H. Shirakawa, M. Araidai, T. Hosoi, H. Watanabe, K. Shiraishi, *Appl. Phys. Express* **2018**, *11*, 061501.
[29] T. Hosoi, K. Watanabe, M. Nozaki, T. Yamada, T. Shimura, H. Watanabe, *Jpn. J. Appl. Phys.* **2019**, *58*, SCCD16.
[30] M.-J. Kang, S.-K. Eom, H.-S. Kim, C.-H. Lee, H.-Y. Cha, K.-S. Seo, *Semicond. Sci. Technol.* **2019**, *34*, 055018.
[31] J. Song, S.-W. Han, H. Luo, J. Rumsey, J. H. Leach, R. Chu, *Appl. Phys. Lett.* **2021**, *119*, 122105.
[32] W. Gonzalez Filho, M. Borga, K. Geens, D. Cingu, U. Chatterjee, S. You, B. Bakeroot, S. Decoutere, W. Knaepen, P. Arnou, P. Homm, in *12th Int. Conf. on Integrated Power Electronics Systems (CIPS)*, **2022**, pp. 1–5.

© 2023 The Authors. Advanced Electronic Materials published by Wiley-VCH GmbH

2199160x, 2024, 3, Downloaded from https://onlinelibrary.wiley.com/doi/10.1002/aelm.202300528 by Cea Grenoble, Wiley Online Library on [20/09/2024]. See the Terms and Conditions (https://onlinelibrary.wiley.com/terms-and-conditions) on Wiley Online Library for rules of use; OA articles are governed by the applicable Creative Commons License

[33] M. Zeghouane, P. Fernandes Paes Pinto Rocha, S. Boubenia, F. Bassani, G. Lefevre, S. Labau, L. Vauche, E. Martinez, M. Veillerot, B. Salem, *AIP Adv.* **2023**, *13*, 085128.
[34] H. B. Profijt, S. E. Potts, M. C. M. van de Sanden, W. M. M. Kessels, *J. Vac. Sci. Technol., A* **2011**, *29*, 050801.
[35] J. L. Van Hemmen, S. B. S. Heil, J. H. Klootwijk, F. Roozeboom, C. J. Hodson, M. C. M. Van De Sanden, W. M. M. Kessels, *J. Electrochem. Soc.* **2007**, *154*, G165.
[36] W. Vandendaele, S. Martin, M.-A. Jaud, A. Krakovinsky, L. Vauche, C. L. Royer, J. Biscarrat, A. G. Viey, R. Gwoziecki, R. Modica, F. Iucolano, M. Plissonnier, F. Gaillard, in *2020 IEEE Int. Electron Devices Meeting (IEDM)*, IEEE, San Francisco, CA **2020**, pp. 23.5.1–23.5.4. https://doi.org/10.1109/IEDM13553.2020.9371965
[37] S. Ozaki, T. Ohki, M. Kanamura, T. Imada, N. Nakamura, N. Okamoto, T. Miyajima, T. Kikkawa, in *2012 Int. Conf. on Compound Semiconductor Manufacturing Technology, CS MANTECH*, Boston, MA **2011**.
[38] Y. Kamada, S. Ozaki, J. Yaita, A. Yamada, T. Ohki, Y. Minoura, Y. Kumazaki, N. Okamoto, K. Makiyama, N. Nakamura, J. Kotani, *Jpn. J. Appl. Phys.* **2020**, *59*, 046505.
[39] J. Robertson, *J. Vac. Sci. Technol. B* **2000**, *18*, 1785.
[40] J. Robertson, *Eur. Phys. J.: Appl. Phys.* **2004**, *28*, 265.
[41] A. Winzer, N. Szabó, A. Wachowiak, P. M. Jordan, J. Heitmann, T. Mikolajick, *J. Vac. Sci. Technol. B* **2015**, *33*, 01A106.
[42] M. Legallais, H. Mehdi, S. David, F. Bassani, S. Labau, B. Pelissier, T. Baron, E. Martinez, G. Ghibaudo, B. Salem, *ACS Appl. Mater. Interfaces* **2020**, *12*, 39870.
[43] P.-M. Deleuze, K. Artyushkova, E. Martinez, O. Renault, *Surf. Sci. Spectra* **2022**, *29*, 014003.
[44] S. G. Rosenberg, D. J. Pennachio, C. Wagenbach, S. D. Johnson, N. Nepal, A. C. Kozen, J. M. Woodward, Z. Robinson, H. Joress, K. F. Ludwig, C. J. Palmstrøm, C. R. Eddy, *J. Vac. Sci. Technol., A* **2019**, *37*, 020908.
[45] P. W. Wang, J.-C. Hsu, Y.-H. Lin, H.-L. Chen, *Surf. Interface Anal.* **2010**, *43*, 1089.
[46] O. Renault, P.-M. Deleuze, J. Courtin, T. R. Bure, N. Gauthier, E. Nolot, C. Robert-Goumet, N. Pauly, E. Martinez, K. Artyushkova, *Faraday Discuss.* **2022**, *236*, 288.
[47] Y. Fujimoto, M. Uenuma, T. Nakamura, M. Furukawa, Y. Ishikawa, Y. Uraoka, *Jpn. J. Appl. Phys.* **2019**, *58*, 040902.
[48] S. Tanuma, C. J. Powell, D. R. Penn, *Surf. Interface Anal.* **1993**, *20*, 13.

© 2023 The Authors. Advanced Electronic Materials published by Wiley-VCH GmbH

2199160x, 2024, 3, Downloaded from https://onlinelibrary.wiley.com/doi/10.1002/aelm.202300528 by Cea Grenoble, Wiley Online Library on [20/09/2024]. See the Terms and Conditions (https://onlinelibrary.wiley.com/terms-and-conditions) on Wiley Online Library for rules of use; OA articles are governed by the applicable Creative Commons License